APPLIED PHYSICS

Thermionic transport across gold-graphene-WSe_2 van der Waals heterostructures

Md Golam Rosul[1], Doeon Lee[1], David H. Olson[2], Naiming Liu[3], Xiaoming Wang[4,5], Patrick E. Hopkins[2,3], Kyusang Lee[1,3], Mona Zebarjadi[1,3]*

Solid-state thermionic devices based on van der Waals structures were proposed for nanoscale thermal to electrical energy conversion and integrated electronic cooling applications. We study thermionic cooling across gold-graphene-WSe_2-graphene-gold structures computationally and experimentally. Graphene and WSe_2 layers were stacked, followed by deposition of gold contacts. The *I-V* curve of the structure suggests near-ohmic contact. A hybrid technique that combines thermoreflectance and cooling curve measurements is used to extract the device *ZT*. The measured Seebeck coefficient, thermal and electrical conductance, and *ZT* values at room temperatures are in agreement with the theoretical predictions using first-principles calculations combined with real-space Green's function formalism. This work lays the foundation for development of efficient thermionic devices.

INTRODUCTION

Solid-state thermionic (SSTI) power generators can be viewed as intermediate between vacuum-state thermionic converters and thermoelectric power generators. Like many other heat engines, these devices can work either as power generators where they convert input heat to electricity or as coolers where applied electricity is used to pump heat. The SSTI power generators and refrigerators were first proposed by Shakouri and Bowers (*1*) and Mahan and Woods (*2*) independently as an alternative to vacuum-state thermionic converters. These devices are made by inserting a semiconducting layer between metallic electrodes. The semiconducting layer forms an energy barrier for charge carriers, allowing only hot ones to pass (*3*–*5*). This current flow is referred to as thermionic current. The SSTI devices are similar to vacuum-state thermionic ones wherein the vacuum is replaced by the semiconducting layer. Because of the lower energy barrier, the SSTI devices operate at temperatures much smaller than the vacuum-state thermionic devices. The SSTI devices are also very similar to thermoelectric devices. The most important difference is that the thermionic transport in SSTI devices is ballistic, whereas the thermoelectric transport is diffusive. Like thermoelectric devices, it is possible to define an equivalent figure of merit, *ZT*, for SSTI devices. The figure of merit concept is borrowed from the thermoelectric field and is defined as $ZT = \frac{\sigma S^2 T}{\kappa}$, where σ is the electrical conductivity, *S* is the Seebeck coefficient, and κ is the thermal conductivity. We note that the energy conversion efficiency and the coefficient of performance equations of SSTI devices are not the same as the ones for thermoelectric devices (*2*, *6*). Only after linearizing the equations (that is, under small temperature drops and small voltage drops), an analogy to thermoelectric modules could be drawn. In this analogy, the Seebeck coefficient is the energy barrier height (in units of volt) divided by the temperature plus a constant. It can be shown numerically that thermoelectric equations can reproduce thermionic results accurately, which is a remarkable observation by Mahan and Woods (*2*). Theoretical investigations had conflicting predictions comparing the efficiency of SSTI converters to those of thermoelectric devices (*1*, *2*, *6*–*8*). In SSTI converters, to maintain ballistic transport of the hot electrons, the semiconducting layer thickness, *L*, should be equal or less than the electron mean free path, λ. On the other hand, a minimum length, L_t, is needed to suppress the tunneling of electrons, which is undesirable because low-energy electrons (with energies smaller than the chemical potential, μ) act as holes and lower the efficiency of the electron transmitting device (similar to bipolar effect in the case of thermoelectric transport). Thus, the semiconducting layer thickness should satisfy the following condition: $L_t < L < \lambda$.

Recently, highly efficient SSTI converters made out of two-dimensional (2D) layered materials were theoretically and computationally proposed (*7*, *9*, *10*). In these structures, the in-plane atoms are covalently bonded, while the layers in the cross-plane direction are weakly bonded by van der Waals forces. Because of weak interlayer bonding, it is possible to stack different 2D materials on top of each other without any strain that would otherwise develop because of lattice mismatch in the presence of a strong bonding (*11*). Bandgap of 2D materials can be tuned by applying strain electric field and also by changing the number of stacked layers. Arsenene, the monolayer of arsenic, for example, has been reported to show a smooth transition from the semimetallic to semiconducting state for different number of stacked layers (*12*). It is also reported that, arsenene, an indirect bandgap semiconductor, can be converted to a direct bandgap semiconductor by applying compressive and tensile strain along its *a* axis (*12*). Another important property of 2D layered heterostructures is their low value of thermal conductance in the cross-plane direction, which is the result of the weak van der Waals interlayer bonding. In SSTI devices, the thermal conductance should be minimized, and extremely small values of 0.1 MW $m^{-2}K^{-1}$ are desirable for achieving high efficiency (*13*). The main challenge is to achieve these small conductance values at small length scales to preserve the ballistic nature of thermionic transport. Extremely small conductance values have already been demonstrated in several 2D layered structures and at nanometer length scales. For example, Yuan *et al.* (*14*) reported thermal conductance values smaller than 1 MW $m^{-2}K^{-1}$ across seven layers of MoS_2. Zhang *et al.* (*15*) estimated the interfacial thermal conductance across monolayer and bilayer $MoSe_2$ to be of the order 0.1 to 1 MW $m^{-2}K^{-1}$. Massicotte *et al.* (*16*) reported a cross-plane thermal conductance of 0.5 MW $m^{-2}K^{-1}$ across the graphene-WSe_2-graphene heterostructure that was tested for photothermionic emission.

[1]Department of Electrical and Computer Engineering, University of Virginia, Charlottesville, VA 22904, USA. [2]Department of Mechanical and Aerospace Engineering, University of Virginia, Charlottesville, VA 22904, USA. [3]Department of Materials Science and Engineering, University of Virginia, Charlottesville, VA 22904, USA. [4]Department of Physics and Astronomy, University of Toledo, Toledo, OH 43606, USA. [5]Wright Center for Photovoltaic Innovation and Commercialization, University of Toledo, Toledo, OH 43606, USA.
*Corresponding author. Email: m.zebarjadi@virginia.edu

Chen *et al.* (*17*) reported a low thermal conductance of 2.36 MW $m^{-2}K^{-1}$ for the graphene–h-BN–graphene heterostructure. In this structure, h-BN forms too high of an energy barrier for electrons and results in poor electronic properties. Therefore, the structure's figure of merit at room temperature is only on the order of 10^{-6}. To our knowledge, this is the only experimentally measured *ZT* for layered structures across few nanometers.

Because of lack of well-established measurement methods (*18*, *19*), currently, there are very few experimental studies focused on the efficiency of the SSTI converters made out of 2D van der Waals heterostructures. Here, we computationally and experimentally study thermionic transport across a gold–graphene–3 layers of WSe_2–graphene–gold (Au-Gr-3WSe_2-Gr-Au) structure. We report a hybrid experimental technique that combines the thermoreflectance and cooling curve measurements to extract the equivalent figure merit of the SSTI converter. Although our measured room temperature figure of merit is small ($ZT = 1.5 \times 10^{-3}$), this value is three orders of magnitude higher than the previously reported value for similar types of 2D heterostructures (*17*). The experimental values are in close agreement with the theoretical values calculated for this structure.

RESULTS

Electrical transport

The Au-Gr-3WSe_2-Gr-Au device was fabricated on the Si/SiO_2 substrate where the device structure is illustrated on Fig. 1A. A bottom graphene layer, three layers of WSe_2, and a top graphene layer were mechanically exfoliated and transferred on the substrate in sequence using a polydimethylsiloxane (PDMS)–assisted transfer method. The thickness of WSe_2 was identified by using optical contrasts on an optical microscope image of the WSe_2 on the PDMS, where thicknesses of reference samples (from one to five layers) were measured by atomic force microscopy (AFM) and their optical contrasts in the green channel of a charge-coupled device camera were served as reference values. Metal electrodes [Ti (3 nm)/Au (100 nm)] were deposited by using a general photolithography process and an electron-beam evaporation. The fabricated device was annealed at 200°C in a vacuum chamber overnight to achieve the ohmic contact between metal and graphene. The optical microscope image of the fabricated device is shown in Fig. 1B, and Fig. 1C shows the current-voltage characteristic measured across the top and bottom metal contacts, indicating a near-ohmic contact. Our further analysis shows that the measured value is dominated by the contact resistance between Au/Ti and graphene (see the Supplementary Materials).

The room temperature Seebeck coefficient of this structure was measured by the setup schematically shown in Fig. 2A. A small external heater was placed close to one of the metallic pads to create a local hot spot. We then used two thermocouples and two electrical probes directly connected to the gold pads (contacts) to simultaneously measure the temperature differential and the Seebeck voltage across the Au-Gr-WSe_2-Gr-Au device. The device-level Seebeck coefficient can be estimated by linearly fitting the measured Seebeck voltage (μV) with respect to the measured temperature differential ΔT (K), as shown in Fig. 2B. It is noted that the data suffer from a large noise due to nonuniformity of the induced temperature gradient across the sample. Nevertheless, our obtained experimental Seebeck coefficient of ~72 ± 12 μV/K is in good agreement with the theoretically calculated value of 84 μV/K using first-principles and Green's function calculations.

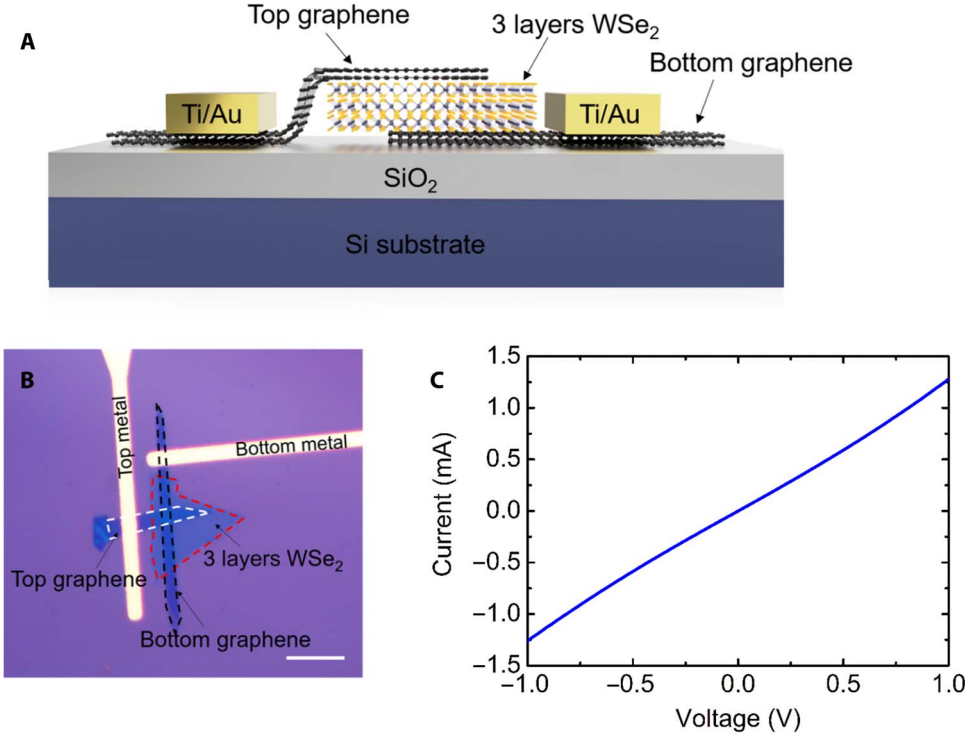

Fig. 1. Au-Gr-3WSe_2-Gr-Au device. (**A**) Illustration of the cross-section of the Au-Gr-3WSe_2-Gr-Au structure. The three layers of WSe_2 flake are sandwiched by top and bottom graphene layers on a Si/SiO_2 substrate, and contact metals (Ti/Au) are deposited on top and bottom graphene layers. (**B**) Optical microscope image of an Au-Gr-3WSe_2-Gr-Au device. The three layers WSe_2, top graphene, and bottom graphene are highlighted by red, white, and black dashed lines, respectively. Scale bar, 20 μm. (**C**) *I-V* curve of the fabricated Au-Gr-3WSe_2-Gr-Au device.

We note that the measured Seebeck coefficient should be interpreted as the device-level Seebeck coefficient and includes contributions from the graphene ribbons and the Gr-3WSe_2-Gr overlap region. While it is not possible to separate the contribution of these two regions, we note that most of the Seebeck signal is from the overlap region. The thermal resistance of the overlap region is much larger than the graphene ribbons; hence, most of the temperature drop is on the overlap region.

Thermionic transport across the Au-Gr-WSe_2-Gr-Au structure with three to five layers of WSe_2 is computationally studied using first-principles calculations combined with real-space Green's function formalism. The schematic of the studied structure is shown in Fig. 3A, and the local density of states (LDOS) of the structure is shown in Fig. 3B. The energy barrier height is about 0.1 eV. It is expected that optimal barrier height for thermionic application is around 2 k_BT (*6*); therefore, it is expected that this device works best at temperatures above 600 K. To reduce the energy barrier, one way is to replace gold with another metal with larger work function. Figure 3C shows the calculated LDOS for platinum with larger work function, which is a better match to the work function of the current structure and hence has a lower energy barrier. In addition, platinum has a larger density of states at the Fermi level, resulting in higher carrier conductance. The electronic transmission function of both gold and platinum structures are shown in Fig. 4A. Both structures show a clear gap when more than three layers of WSe_2 are present, indicating that three layers are enough to suppress the tunneling current. Using the density of state and the transmission function, the electronic transport properties could be

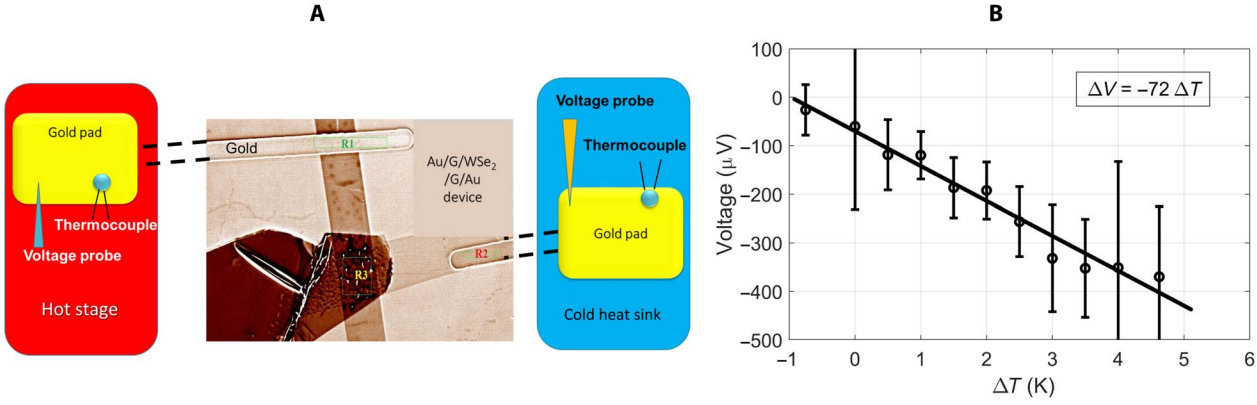

Fig. 2. Seebeck measurement. (**A**) Schematic of the Seebeck measurement setup. (**B**) Seebeck voltage measured versus applied temperature difference. The measured Seebeck coefficient is 72 ± 12 μV/K.

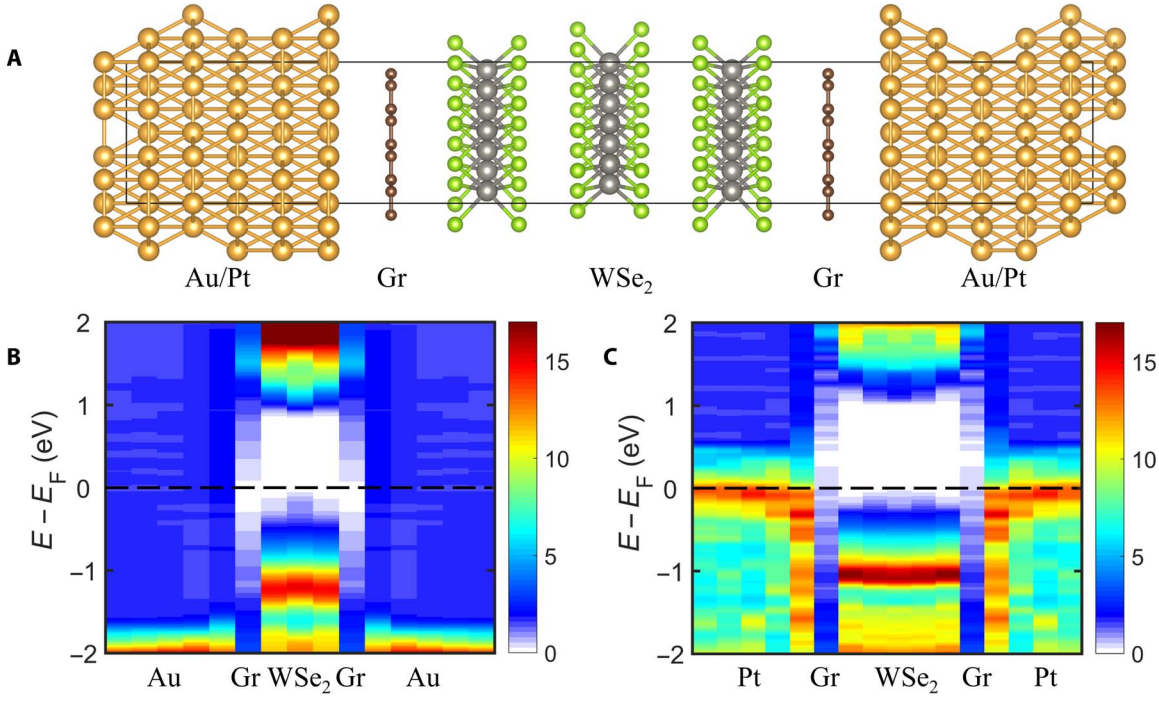

Fig. 3. Electronic structure of Au/Pt-Gr-WSe_2-Gr-Au/Pt. (**A**) Ball-stick model for the configuration of Au/Pt-Gr-WSe_2-Gr-Au/Pt. The yellow, green, gray, and brown balls denote Au/Pt, Se, W, and C atoms, respectively. (**B**) Contour plot of the LDOS of the Au-Gr-WSe_2-Gr-Au structure. The horizontal axis shows the positions of different layers. (**C**) Contour plot of the LDOS of the Pt-Gr-WSe_2-Gr-Pt structure. The horizontal axis shows the positions of different layers.

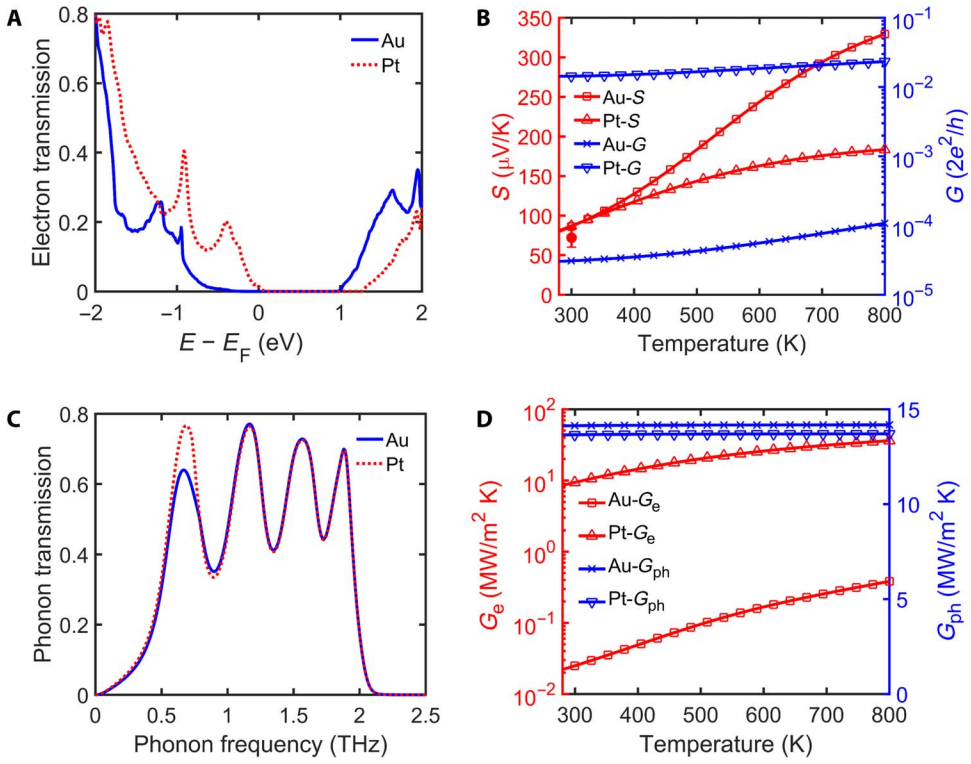

Fig. 4. Transport properties of Au/Pt-Gr-WSe$_2$-Gr-Au/Pt. (**A**) Electron transmission function in the cross-plane direction of gold structure (solid blue line) and platinum structure (red dotted line). (**B**) Calculated Seebeck coefficient (*S*, red line) and electrical conductance (*G*, blue line) versus temperature of both gold and platinum structure. The red circle is the experimentally measured Seebeck coefficient at room temperature. (**C**) Phonon transmission function in the cross-plane direction of gold structure (solid blue line) and platinum structure (red dotted line). (**D**) Calculated electronic thermal conductance (G_e, red line) and lattice thermal conductance (G_{ph}, blue line) versus temperature of both gold and platinum structure.

calculated using linear response integrals. The results indicate a very small electrical conductance value of 3.5×10^{-5} in units of quantum conductance for the Au-Gr-3WSe$_2$-Gr-Au structure. This value is equivalent to resistance times area of $3.7\times10^{-10}\Omega m^2$, which is too small for an efficient performance. The conductance is greatly enhanced when gold is replaced by platinum, as shown in Fig. 4B, due to the lower energy barrier of the platinum structure. The calculated equivalent Seebeck coefficient of the Au-Gr-3WSe$_2$-Gr-Au structure is 84 μV/K at room temperatures, consistent with our experimentally measured value, and increases up to 292 μV/K at high temperatures ($T \sim 700$ K).

Thermal transport

Because of the large size of the supercell, full first-principles calculations of lattice thermal conductance values are too costly for the current structure. Therefore, we used a simpler 1D model as described in our previous publication (*9*). The calculated phonon thermal conductance of Au-Gr-3WSe$_2$-Gr-Au is about 14 MW m^{-2}K^{-1}. Because of the ballistic nature of transport, at temperatures above 200 K, the thermal conductance values do not change substantially, as shown in Fig. 4D. The electronic part of the thermal conductance is an order of magnitude smaller compared to the lattice part at room temperatures but reaches 0.2 MW m^{-2}K^{-1} at 680 K. Last, overall, *ZT* is small. The calculated electronic and phononic transmission functions, the Seebeck coefficient, and the electrical and thermal conductance are shown in Fig. 4. As mentioned, the small electronic conductance is the main drawback of the current structure. To demonstrate the importance of the metallic contact, we also report theoretical results of replacing gold with platinum. Because of improved conductance values, the platinum structure shows a much larger *ZT* values, as shown in the Supplementary Materials.

To check the validity of theory, we used time domain thermoreflectance (TDTR) measurements to experimentally measure the thermal conductance of the fabricated device (*20*). We deposit a nominal 80-nm-thick aluminum layer via electron-beam evaporation to serve as transducer for the Gr-3WSe$_2$-Gr device. The measured resistance thus encompasses contributions from the Al-Gr interface, the Gr-3WSe$_2$-Gr structure, and the Gr-SiO$_2$ interface. The measured conductance accounting for each of these contributions is determined to be 9 MW m^{-2}K^{-1}. We also measured the conductance of the Al-Gr-SiO$_2$ interface and determine this to be 20 MW m^{-2} K^{-1}. Using a series resistor model, discussed further in the Supplementary Materials, the thermal conductance of the Gr-WSe$_2$-Gr layer can be extracted to be 17 MW m^{-2}K^{-1}. This is in good agreement with the theoretically calculated value. We note that the Au-Gr contacts are not included in the experiment, and if included, they will lower the overall thermal conductance value.

Last, we evaluate the device-level *ZT* by directly measuring the cooling curve of the device using a thermoreflectance imaging technique. We borrow the cooling curve concept from the thermoelectric field. This measurement is done routinely for testing the device performance of thermoelectric devices. The principle is as follows: A temperature difference develops as a result of applying an electric current to a Peltier module. This temperature difference is due to the Peltier effect and the Joule heating. The temperature difference is measured at steady state for

a range of applied currents. It is shown that the maximum cooling (ΔT_m) is achieved when the cold side is fully isolated (zero heat flux), the hot side is connected to a heat sink (constant temperature boundary conditions), and the current is equal to $I_{opt} = \frac{ST_C}{R}$, where T_C is the temperature on the cold side and R is the resistance of the device. Under these conditions, ΔT_m is proportional to the ZT of the device following Eq. 1 (*21*, *22*)

$$ZT = \frac{2\Delta T_m}{T_c} \quad (1)$$

To perform cooling curve measurements, we use a thermoreflectance technique, wherein a pulsed voltage is applied across the device and the 2D temperature profile of the device is obtained by mapping the local changes in the reflectance coefficient to the local temperature. To help visually perceive the thermal condition in the device under bias for thermoreflectance imaging, we demonstrate the temperature mapping of the device under a relatively large pulsed voltage of 2 V, as shown in Fig. 5A. Joule heating of up to 9°C is observed at the top surface of the Gr-WSe_2-Gr junction. The hot spots indicate the inhomogeneity or defects at the interface. It is observed that the heat is mostly generated in the active layers and leaks through the graphene ribbons and gold contacts.

Figure 5B shows the cooling curve obtained by using a thermoreflectance imaging technique under low bias voltages up to ~0.06 V. Using Eq. 1, we can estimate an equivalent ZT to be 1.5×10^{-3} for the Au-Gr-3WSe_2-Gr-Au structure. The boundary conditions used to obtain Eq. 1 is not satisfied in our experiment. First, the device is fabricated on a SiO_2 layer, which cannot dissipate the heat effectively and cannot serve as a perfect heat sink. Second, the cold side is not thermally isolated, and there is a small heat leak due to convection, because the measurement is not performed in vacuum. Therefore, our measured ZT is considered to be underestimated for this device structure. While still too small for practical application, our measured ZT already shows three-order-of-magnitude enhancement compared with the previously reported ZT values for similar nanometer-thick 2D layered heterostructures (*17*).

DISCUSSION

To summarize, we have used first-principles calculations combined with Green's function formalism to estimate the thermionic performance of Au-Gr-1 to five layers of WSe_2-Gr-Au structures. We further fabricated the device and measured its performance to validate the theory. The calculated transmission function indicated a clear suppression of tunneling current for structures with more than three layers of WSe_2. Therefore, three layers are enough to build a thermionic device. The calculated barrier height is 0.1 eV, indicating that this device operates best at temperatures above 600 K. The electronic conductance and the Seebeck coefficient both increase with temperature, as shown in Fig. 4B. The room temperature calculated Seebeck coefficient is in close agreement with the experimentally measured value of 72 μV/K, signifying the accuracy of the calculations.

In the cross-plane direction, the thermal conductivity of the WSe_2-layered structure has been reported to be as low as 0.05 W m^{-1} K^{-1}, which is among the lowest possible thermal conductivity values in solid (*23*). This ultralow thermal conductivity, along with the large thermal boundary resistance values reported for interfaces of 2D layered heterostructures, points to small values for the thermal conductance of the studied structure.

The calculated lattice thermal conductance of 14 MW $m^{-2}K^{-1}$ for Au-Gr-3WSe_2-G-Au is close to the measured value of 17 MW $m^{-2}K^{-1}$ for Gr-3WSe_2-Gr. The thermal conductance at Au-Gr contacts is low and is about 20 MW $m^{-2}K^{-1}$. It is shown that the limited phonon density of states in Au is the determining factor in thermal transport at Au-Gr interfaces (*24*, *25*). If we add the thermal resistance of the Au-Gr contacts in series to Gr-3WSe_2-Gr, we obtain a value of 6.3 MW m^{-2} K^{-1}. The experimentally measured conductance value is smaller than the theoretically calculated ones due to the inevitable presence of defects. Values for similar structures have been reported in the literature. Massicotte *et al.* (*16*) reported a conductance of 0.5 MW m^{-2} K^{-1} for Au-Gr-4WSe_2-Gr-Au. However, we note that the conductance reported reflects that of electron-phonon coupling at Gr-hBN interfaces, a parallel process to the phonon-mediated conductance across these interfaces. Thus, we cannot make direct comparisons between values determined in our work and those found in the literature. The contribution of electron-phonon coupling to the conductance of three- and

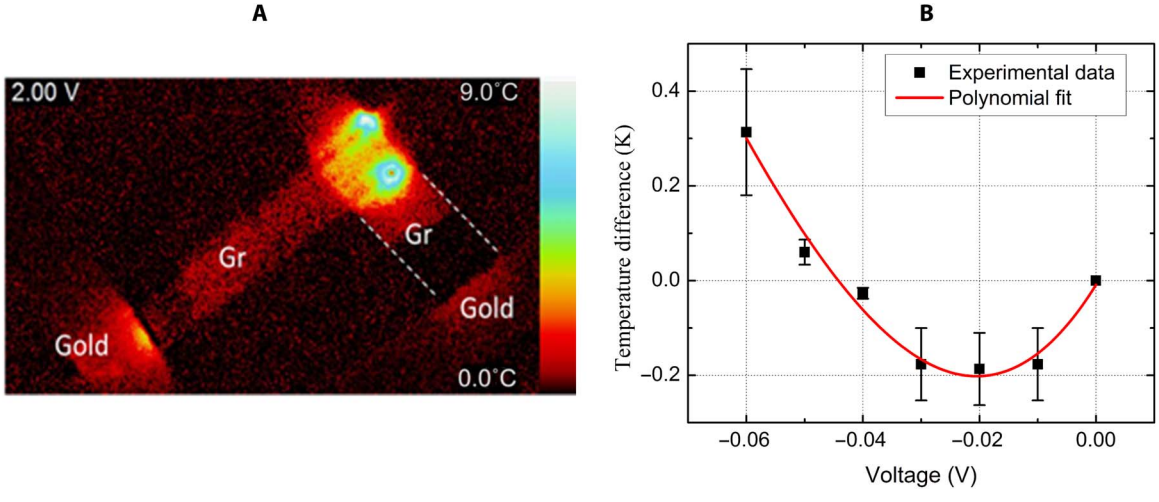

Fig. 5. Thermal imaging of the Joule heating inside the structure and cooling curve. (**A**) Joule heating: 2D temperature map of the Au-Gr-WSe_2-Gr-Au device under a relatively high-voltage 2 V obtained using the thermoreflectance method. Joule heating dominates in the Gr-WSe_2-Gr junction and leaks through the graphene ribbon and gold contacts. (**B**) Cooling curve: Temperature difference between the substrate and top of the active device in Kelvin versus applied voltage at small applied voltages.

four-layer WSe_2 is reported to be similar due to the ballistic nature of transport in these layers (*16*); however, the total thermal conductance across metal-WSe_2-substrate interfaces has been shown to decrease following an increase in the number of WSe_2 layers (*26*). The trend in the latter is consistent with the ultralow thermal conductivity of WSe_2 (*23*), as the resistances compound following an increase in the number of layers.

The *I*-*V* curve of the fabricated structure indicates a near-ohmic contact. The overall electrical conductance value calculated for the Au-Gr-3WSe_2-Gr-Au structure is small. For the fabricated structure with an area of approximately 3 μm × 3 μm, the resistance is about 40 ohms. Our contact resistance measurements indicate that the Au-Ti-Gr contact varies from device to device and has a range from 0.5 to 2 kilohms. That is, contact resistance is the dominant resistance in the experiment. If we use the measured Seebeck coefficient, the calculated resistance, and the measured thermal conductance, then we obtain a ZT of 7×10^{-4} for the current structure, which is twice smaller than the directly measured ZT value using thermoreflectance measurements. There are many sources of error when calculating ZT from the three transport properties. First, while TDTR measurements are reliable for these measurements, we used resistive model to add the thermal resistance of Au-Gr and Gr-3WSe_2-Gr, which only gives a rough idea about the overall thermal resistance of the device. Second, we were not able to extract the electrical conductance of the device due to the large contact resistance, and hence, we used the theoretical value for it. Last, there are sample variations due to the presence of defects, and we note that the TDTR measurement was performed on a different sample.

The directly measured ZT value using the thermoreflectance method, 1.5×10^{-3}, is small, but it is substantially larger compared with other similar structures. We have recently measured ZT of monolayer and bilayer WSe_2 layers sandwiched between gold and graphite and only observed ZT values on the order of 10^{-5} due to the dominance of the tunneling current. Similarly, ZT of Gr-hBN-Gr is reported to be on the order of 10^{-6}. Our measured ZT value is also consistent with the small calculated ZT values for this structure at room temperatures. As discussed before, the studied structure is suitable for elevated temperatures. To improve the ZT values at room temperatures, structures with lower electron energy barriers are needed. The barrier height of the current structure is 0.1 eV. If we replace the gold contacts with another metal that can form a lower energy barrier (~0.05 eV), then we can extend the high performance of the device to room temperatures. We studied several possible metals. The most promising one for this structure is platinum. Transport properties of Pt-Gr-3WSe_2-Gr-Pt are reported in Fig. 4. The main advantage of Pt is to lower the energy barrier and therefore improve the electrical conductance. As shown in Fig. 4B, a two-order-of-magnitude enhancement in the electrical conductance is expected when replacing Au with Pt without impairing other transport properties.

MATERIALS AND METHODS

Device fabrication

A bottom graphene layer, three layers of WSe_2, and a top graphene layer were mechanically exfoliated and transferred on the substrate in sequence using a PDMS-assisted transfer method. The thickness of WSe_2 was identified by using optical contrasts on an optical microscope image of the WSe_2 on the PDMS, where thicknesses of reference samples (from one to five layers) were measured by AFM and their optical contrasts in the green channel of a charge-coupled device camera were served as reference values. Metal electrodes (Ti/Au, 3 nm/100 nm) were deposited by using a general photolithography process and an electron-beam evaporation. The fabricated device was annealed at 200°C on a vacuum chamber overnight to achieve the ohmic contact between metal and graphene.

Transport characterization

The *I*-*V* curve of the device was measured using the two-probe method. The thermoreflectance measurement is based on the relative change in the reflectivity (due to change of refractive index) of a device surface as a function of change in temperature, which can be represented by the following first-order relationship (*27*)

$$\frac{\Delta R}{R_o} = \left(\frac{1}{R_o}\frac{\delta R}{\delta T}\right)\Delta T = C_{th}\Delta T$$

where ΔR is the change in reflectivity, R is the reflected light, C_{th} is the thermoreflectance calibration coefficient, and ΔT is the change in temperature. The calibration coefficient is typically of the order of 10^{-2} to 10^{-5} and dependent on the sample material, the wavelength of the illuminating light, the angle of incidence (and thus, by extension, the surface roughness), and the composition of the sample in the case of multilayer structures. Therefore, calibration for each material is required to determine the exact value of calibration coefficient. The calibration method consists of heating the sample using an external thermoelectric heating stage and a microthermocouple to record the induced temperature change. The sample is heated at two distinct temperatures, where the reflectance distribution of the surface is measured. By measuring the change in reflectance, the thermoreflectance coefficient can be calculated at each location across the sample surface. The measured calibration coefficient using 530-nm light-emitting diode (LED) on the overlap region of our sample was 2.0 (± 0.3) × 10^{-4}.

Thermoreflectance measurement was carried out on the sample using the Microsanj NT220B system. The thermoreflectance measurement system consists of a pulse generator, a signal generator, and a control unit. A 530-nm green LED was used as an illuminator and was focused onto the sample's top surface through a beam splitter and a high-magnification objective. The reflected light that contained the information on the sample surface temperature change was collected by a charge-coupled device detector. A 100-μs voltage pulse was applied to the metallic contacts, and the temperature response of the sample was measured at 90 μs. Steady-state conditions were achieved after 50 to 70 μs.

We used TDTR to characterize the conductance of the Gr-3WSe_2-Gr structure. Our two-tint implementation of the technique was discussed elsewhere in the literature (*20*), along with the associated analysis of the technique (*28*–*30*). We first coated a nominal 80-nm Al transducer onto our Gr-3WSe_2-Gr structure, which had been mechanically exfoliated previously onto silicon with a thermal oxide of 300 nm. The thickness of the Al was confirmed via picosecond acoustics (*31*, *32*), while its thermal conductivity was determined from reference specimens placed near the Gr-3WSe_2-Gr sample during deposition. The effective $1/e^2$ pump/probe radius is ~1.5 μm. The measured conductance at the Al-Gr-SiO_2 interface was found to be 20 MW m^{-2} K^{-1}, while that of the Al-Gr-3WSe_2-Gr-SiO_2 interfaces was 9 MW m^{-2} K^{-1}. Because these two measurements reflect the series resistances of the structures, we can use these values to determine the thermal conductance of the Gr-3WSe_2-Gr

structure alone. Doing so allowed us to extract a conductance of 17 MW m^{-2} K^{-1} for the structure.

Computational methods

To study the structural and electronic properties of the Au-Gr-WSe_2-Gr-Au van der Waals heterostructure, we used the state-of-the-art density functional theory–based first-principles calculations, as implemented in the SIESTA package (*33*). We used the exchange-correlation functional of Perdew-Burke-Ernzerhof (*34*) revised for solids (*35*) and standard basis set, namely, double zeta plus polarization. Real-space mesh cutoff energy was set to 300 rydberg. A single k point in the cross-plane direction and a 5 × 5 k mesh in the basal plane were used for the Brillouin zone sampling. The in-plane lattice constants were fixed to the relaxed gold <111> plane, while the graphene and WSe_2 lattices were adapted accordingly ($2\sqrt{3}a_{Au<111>} = 4a_{Gr} = \sqrt{7}a_{WSe_2}$, a is the lattice constant). The cross-plane direction was relaxed without any constraint. The forces of all the atoms were relaxed within 0.01 eV/Å. The ballistic transport properties were calculated using the real-space Green's function method as in the TranSIESTA implementation (*36*). Phonon thermal conductance was calculated using the Green's function method simplified for 1D model (*9*).

SUPPLEMENTARY MATERIALS

Supplementary material for this article is available at http://advances.sciencemag.org/cgi/content/full/5/11/eaax7827/DC1

Section S1. Series resistor model
Section S2. Analysis of contact resistance
Fig. S1. TDTR measurement.
Fig. S2. Figure of merit (ZT) of Au-G-WSe_2-G-Au structure and Pt-G-WSe_2-G-Pt structure.
Fig. S3. Repeatable cooling curve measurement.
Fig. S4. Contact resistance measurement.
Table S1. Two-probe resistance data for samples 1 and 2.
Table S2. Four-probe resistance data for samples 1 and 2.
Table S3. Contact resistances.

REFERENCES AND NOTES

1. A. Shakouri, J. E. Bowers, Heterostructure integrated thermionic coolers. *Appl. Phys. Lett.* **71**, 1234–1236 (1997).
2. G. D. Mahan, L. M. Woods, Multilayer thermionic refrigeration. *Phys. Rev. Lett.* **80**, 4016–4019 (1998).
3. M. Markov, M. Zebarjadi, Thermoelectric transport in graphene and 2D layered materials. *Nanoscale Microscale Thermophys. Eng.* **23**, 117–127 (2018).
4. Y. Hishinuma, T. H. Geballe, B. Y. Moyzhes, T. W. Kenny, Refrigeration by combined tunneling and thermionic emission in vacuum: Use of nanometer scale design. *Appl. Phys. Lett.* **78**, 2572–2574 (2001).
5. G. Chen, A. Shakouri, Heat transfer in nanostructures for solid-state energy conversion. *J. Heat Transfer* **124**, 242–252 (2002).
6. G. D. Mahan, J. O. Sofo, M. Bartkowiak, Multilayer thermionic refrigerator and generator. *J. Appl. Phys.* **83**, 4683–4689 (1998).
7. S.-J. Liang, B. Liu, W. Hu, K. Zhou, L. K. Ang, Thermionic energy conversion based on graphene van der Waals heterostructures. *Sci. Rep.* **7**, 46211 (2017).
8. C. B. Vining, G. D. Mahan, The B factor in multilayer thermionic refrigeration. *J. Appl. Phys.* **86**, 6852–6853 (1999).
9. X. Wang, M. Zebarjadi, K. Esfarjani, First principles calculations of solid-state thermionic transport in layered van der Waals heterostructures. *Nanoscale* **8**, 14695–14704 (2016).
10. X. Wang, M. Zebarjadi, K. Esfarjani, High-performance solid-state Thermionic energy conversion based on 2D van der Waals heterostructures: A first-principles study. *Sci. Rep.* **8**, 9303 (2018).
11. Y. Liu, N. O. Weiss, X. Duan, H.-C. Cheng, Y. Huang, X. Duan, Van der Waals heterostructures and devices. *Nat. Rev. Mater.* **1**, 16042 (2016).
12. C. Kamal, M. Ezawa, Arsenene: Two-dimensional buckled and puckered honeycomb arsenic systems. *Phys. Rev. B* **91**, 085423 (2015).
13. M. Zebarjadi, Solid-state thermionic power generators: An analytical analysis in the nonlinear regime. *Phys. Rev. Appl.* **8**, 014008 (2017).
14. P. Yuan, C. Li, S. Xu, J. Liu, X. Wang, Interfacial thermal conductance between few to tens of layered-MoS_2 and c-Si: Effect of MoS_2 thickness. *Acta Mater.* **122**, 152–165 (2017).
15. X. Zhang, D. Sun, Y. Li, G.-H. Lee, X. Cui, D. Chenet, Y. You, T. F. Heinz, J. C. Hone, Measurement of lateral and interfacial thermal conductivity of single- and bilayer MoS_2 and $MoSe_2$ using refined optothermal Raman technique. *ACS Appl. Mater. Interfaces* **7**, 25923–25929 (2015).
16. M. Massicotte, P. Schmidt, F. Vialla, K. Watanabe, T. Taniguchi, K. J. Tielrooij, F. H. L. Koppens, Photo-thermionic effect in vertical graphene heterostructures. *Nat. Commun.* **7**, 12174 (2016).
17. C.-C. Chen, Z. Li, L. Shi, S. B. Cronin, Thermoelectric transport across graphene/hexagonal boron nitride/graphene heterostructures. *Nano Res.* **8**, 666–672 (2015).
18. Z. Li, S. R. Bauers, N. Poudel, D. Hamann, X. Wang, D. S. Choi, K. Esfarjani, L. Shi, D. C. Johnson, S. B. Cronin, Cross-plane Seebeck coefficient measurement of misfit layered compounds $(SnSe)_n(TiSe_2)_n$ (n = 1,3,4,5). *Nano Lett.* **17**, 1978–1986 (2017).
19. N. Poudel, S.-J. Liang, D. Choi, B. Hou, L. Shen, H. Shi, L. K. Ang, L. Shi, S. Cronin, Cross-plane thermoelectric and thermionic transport across Au/h-BN/graphene heterostructures. *Sci. Rep.* **7**, 14148 (2017).
20. K. Kang, Y. K. Koh, C. Chiritescu, X. Zheng, D. G. Cahill, Two-tint pump-probe measurements using a femtosecond laser oscillator and sharp-edged optical filters. *Rev. Sci. Instrum.* **79**, 114901 (2008).
21. H. J. Goldsmid, *Introduction to Thermoelectricity* (Springer Series in Materials Science, Springer, 2009).
22. A. V. da Rosa, *Fundamentals of Renewable Energy Processes* (Elsevier, ed. 3, 2013).
23. C. Chiritescu, D. G. Cahill, N. Nguyen, D. Johnson, A. Bodapati, P. Keblinski, P. Zschack, Ultralow thermal conductivity in disordered, layered WSe_2 crystals. *Science* **315**, 351–353 (2007).
24. Y. K. Koh, M.-H. Bae, D. G. Cahill, E. Pop, Heat conduction across monolayer and few-layer graphenes. *Nano Lett.* **10**, 4363–4368 (2010).
25. P. E. Hopkins, M. Baraket, E. V. Barnat, T. E. Beechem, S. P. Kearney, J. C. Duda, J. T. Robinson, S. G. Walton, Manipulating thermal conductance at metal–graphene contacts via chemical functionalization. *Nano Lett.* **12**, 590–595 (2012).
26. Y. G. Choi, D. G. Jeong, H. I. Ju, C. J. Roh, G. Kim, B. S. Mun, T. Y. Kim, S.-W. Kim, J. S. Lee, Covalent-bonding-induced strong phonon scattering in the atomically thin WSe_2 layer. *Sci. Rep.* **9**, 7612 (2019).
27. D. Kendig, K. Yazawa, A. Shakouri, Hyperspectral thermoreflectance imaging for power devices, in *Proceedings of the 33rd Thermal Measurement, Modeling & Management Symposium (SEMI-THERM)* (IEEE, 2017), pp. 204–207.
28. A. J. Schmidt, X. Chen, G. Chen, Pulse accumulation, radial heat conduction, and anisotropic thermal conductivity in pump-probe transient thermoreflectance. *Rev. Sci. Instrum.* **79**, 114902 (2008).
29. D. G. Cahill, Analysis of heat flow in layered structures for time-domain thermoreflectance. *Rev. Sci. Instrum.* **75**, 5119–5122 (2004).
30. P. E. Hopkins, J. R. Serrano, L. M. Phinney, S. P. Kearney, T. W. Grasser, C. T. Harris, Criteria for cross-plane dominated thermal transport in multilayer thin film systems during modulated laser heating. *J. Heat Transfer* **132**, 81302 (2010).
31. C. Thomsen, H. J. Maris, J. Tauc, Picosecond acoustics as a non-destructive tool for the characterization of very thin films. *Thin Solid Films* **154**, 217–223 (1987).
32. G. T. Hohensee, W. P. Hsieh, M. D. Losego, D. G. Cahill, Interpreting picosecond acoustics in the case of low interface stiffness. *Rev. Sci. Instrum.* **83**, 114902 (2012).
33. J. M. Soler, E. Artacho, J. D. Gale, A. García, J. Junquera, P. Ordejón, D. Sánchez-Portal, The SIESTA method for ab initio order-N materials simulation. *J. Phys. Condens. Matter* **14**, 2745–2779 (2002).
34. J. P. Perdew, K. Burke, M. Ernzerhof, Generalized gradient approximation made simple. *Phys. Rev. Lett.* **77**, 3865–3868 (1996).
35. J. P. Perdew, A. Ruzsinszky, G. I. Csonka, O. A. Vydrov, G. E. Scuseria, L. A. Constantin, X. Zhou, K. Burke, Restoring the density-gradient expansion for exchange in solids and surfaces. *Phys. Rev. Lett.* **100**, 136406 (2008).
36. M. Brandbyge, J.-L. Mozos, P. Ordejon, J. Taylor, K. Stokbro, Density-functional method for nonequilibrium electron transport. *Phys. Rev. B* **65**, 165401 (2002).

Acknowledgments: This publication is dedicated to the memory of Mildred Dresselhaus (1930–2017), who served the scientific community not only with her broad knowledge of physics and science policy but also by empowering young scientists from diverse backgrounds. She was a role model and a source of inspiration for the scientific community including the authors of this paper. **Funding:** This work was supported by the National Science Foundation grant no. 1653268 (to M.G.R., N.L. and M.Z.) and UVA Research Innovation award grant no. 158670 (to M.Z., K.L., and D.L.). This manuscript is based upon work supported by the Air Force Office of Scientific Research under award no. FA9550-18-1-0352. D.H.O. is grateful for the support from the National

Defense Science and Engineering Graduate (NDSEG) Fellowship. **Author contributions:** M.Z. proposed and supervised the project. D.L. and K.L. designed and fabricated the structure. M.G.R. and N.L. performed the transport measurements. X.W. did the computational analysis. D.H.O. and P.E.H. performed the thermal conductance TDTR measurements. All authors contributed to the writing of the paper. **Competing interests:** The authors declare that they have no competing interests. **Data and materials availability:** All data needed to evaluate the conclusions in the paper are present in the paper and/or the Supplementary Materials. Additional data related to this paper may be requested from the authors.

Submitted 1 May 2019
Accepted 17 September 2019
Published 8 November 2019
10.1126/sciadv.aax7827

Citation: M. G. Rosul, D. Lee, D. H. Olson, N. Liu, X. Wang, P. E. Hopkins, K. Lee, M. Zebarjadi, Thermionic transport across gold-graphene-WSe_2 van der Waals heterostructures. *Sci. Adv.* **5**, eaax7827 (2019).

Science Advances

Thermionic transport across gold-graphene-WSe_2 van der Waals heterostructures

Md Golam Rosul, Doeon Lee, David H. Olson, Naiming Liu, Xiaoming Wang, Patrick E. Hopkins, Kyusang Lee and Mona Zebarjadi

Sci Adv **5** (11), eaax7827.
DOI: 10.1126/sciadv.aax7827